"Efficient optimization methodology for laser powder bed fusion parameters to manufacture dense and mechanically sound parts validated on AlSi12 alloy"

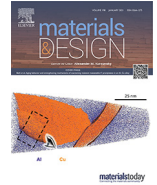Gheysen, Julie ; Marteleur, Matthieu ; van der Rest, Camille ; Simar, Aude

ABSTRACT

Themain drawback of laser powder bed fusion (L-PBF), commonly called selective lasermelting (SLM) is the high porosity which may lead to an early failure of the parts. To minimize it, the L-PBF parameters need to be optimized focusing on the laser power, scanning speed and hatching space. However, no standard guideline exists. In this study, an efficient and cost-effective methodology is developed and validated on AlSi12. This innovative methodology brings together single scan tracks (SST),macroscopic properties analysis and design of experiments (DOE). It requires three batches of SST, cubes and tensile samples. The DOE significantly decreases the manufacturing and characterization costs. 9 SST are sufficient to identify a process window that is 85% similar to the one obtained froma full factorial designwith 105 SST. This process windowreliably leads to high densities and better mechanical properties in comparison to the state-of-the-art properties reported in the literature for L-PBF AlSi12. In conclusion, a methodology using only 9 SST, 18 cubes and 12 tensile tests has been validated on AlSi12. It is further envisioned to optimize the L-PBF parameters of any existing or new alloy leading potentially towards better mechanical properties than the state-of-the-art in the literature.

CITE THIS VERSION

Efficient optimization methodology for laser powder bed fusion parameters to manufacture dense and mechanically sound parts validated on AlSi12 alloy
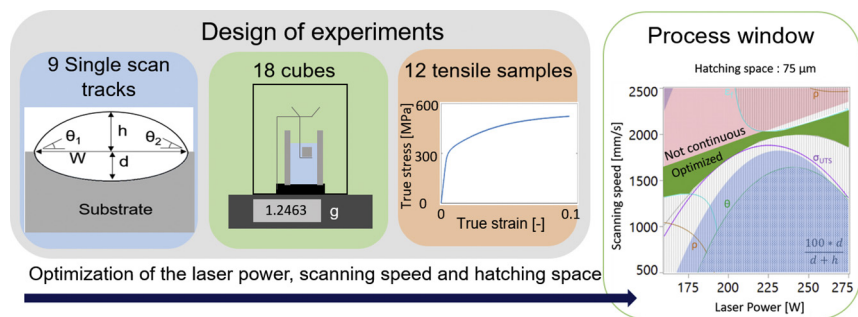
Julie Gheysen *, Matthieu Marteleur, Camille van der Rest, Aude Simar

Université Catholique de Louvain, Institute of Mechanics, Materials and Civil Engineering, Place Sainte-Barbe 2, 1348 Louvain-la-Neuve, Belgium

HIGHLIGHTS

- The optimum L-PBF parameters have been established for AlSi12 based on an efficient and cost-effective methodology.
- The methodology only requires 9 single scan tracks (SST), 18 cubes and 12 tensile samples to optimize the L-PBF parameters.
- 9 SST identifies a process window 85% similar to the one resulting from a full factorial design with 105 SST.
- The process window obtained based on the 9 SST leads to high-density (> 99.3%), proving the relevance of the SST.
- The optimum L-PBF parameters lead to better static mechanical properties than the state-of-the-art ones reported in literature for L-PBF AlSi12.

GRAPHICAL ABSTRACT

ARTICLE INFO

ABSTRACT

The main drawback of laser powder bed fusion (L-PBF), commonly called selective laser melting (SLM) is the high porosity which may lead to an early failure of the parts. To minimize it, the L-PBF parameters need to be optimized focusing on the laser power, scanning speed and hatching space. However, no standard guideline exists. In this study, an efficient and cost-effective methodology is developed and validated on AlSi12. This innovative methodology brings together single scan tracks (SST), macroscopic properties analysis and design of experiments (DOE). It requires three batches of SST, cubes and tensile samples. The DOE significantly decreases the manufacturing and characterization costs. 9 SST are sufficient to identify a process window that is 85% similar to the one obtained from a full factorial design with 105 SST. This process window reliably leads to high densities and better mechanical properties in comparison to the state-of-the-art properties reported in the literature for L-PBF AlSi12. In conclusion, a methodology using only 9 SST, 18 cubes and 12 tensile tests has been validated on AlSi12. It is further envisioned to optimize the L-PBF parameters of any existing or new alloy leading potentially towards better mechanical properties than the state-of-the-art in the literature.

* Corresponding author at: Place Ste-Barbe 2 L5.02.02, Louvain-la-Neuve 1348, Belgium.
E-mail address: julie.gheysen@uclouvain.be (J. Gheysen).

1. Introduction

Laser powder bed fusion (L-PBF) is an additive manufacturing process also commonly called selective laser melting (SLM). Based on a computer-aided design model, it allows the manufacturing of complex and customized geometries, which are not always possible with conventional techniques. A laser beam melts layer-by-layer the region of the powder bed corresponding to the manufactured part. The main drawback of this technique is the high porosity level in the final product that can lead to an early failure of the component [1].

Many physical phenomena are involved in this process such as laser absorption, heat transfer, Marangoni convection and material evaporation. Qiu et al. [1] showed that these phenomena influence the melt flow and ultimately, the development of porosity. Their prominence depends on the L-PBF parameters and mainly on the laser power (P), the scanning speed (v), the layer thickness (t) and the hatching space (HS). It is therefore critical to optimize these four L-PBF parameters in order to manufacture dense parts.

Many studies have optimized the L-PBF parameters for different materials with the aim of minimizing the porosity. Most of them manufacture cubes with different L-PBF parameters and select finally those leading to the highest density measured by Archimedes density method. This procedure was applied for tungsten [2], AlSi10Mg [3], HY100 steel [4], etc. This technique is not efficient as it is time and material consuming to manufacture and test all these cubes. Moreover, at the end, optimal parameters might not be evidenced.

To tackle these issues, some researches successfully used statistical analysis and design of experiments (DOE), usually response surface method (RSM), to evaluate the significance and the influence of the L-PBF parameters on the quality of the parts such as the porosity level and the roughness. According to Montgomery et al. [5] "*The RSM is a collection of mathematical and statistical techniques useful for the modelling and analysis of problems in which a response of interest is influenced by several variables and the objective is to optimize this response.*" This procedure was applied successfully for Ni-superalloy [6], Ti-6Al-4 V [7], AZ31 magnesium [8], etc. The advantage of using DOE is that the optimal parameters might be evidenced and that it is less time consuming than the previous approach.

Another approach based on the single scan tracks (SST) analysis was developed and already applied for AlSi10Mg [9], AlSi10Mg + 4Cu [10], Ti-40Al-9 V-0.5Y [11], pure tungsten [12], Al-Cu-Mg [13], steel 316 L [14] and Inconel 625 [14]. The idea is that L-PBF parts are made of overlapping SST, therefore the properties of the part strongly depend on the properties of each SST. This approach focuses on optimizing the geometry of the track by playing with the most significant L-PBF parameters: the laser power P and the scanning speed v. Yadroitsev et al. [14] showed that when the linear energy density E_L, defined by Eq. 1, is too low to melt the substrate, the track becomes a series of drops due to poor wetting of the melt, called *balling phenomena*.

$$E_L = P/v \qquad (1)$$

When E_L is too high, instabilities appear as distortions and irregularities. The optimal parameters leading to stable SST are in between these two lower and upper energy bounds. Moreover, they showed that the range of optimal scanning speed is wider for high laser power. Aversa et al. [9] defined the process window of AlSi10Mg based on five types of SST in function of the top view and cross sections analysis: 1) too low energy to melt the powder, 2) balling phenomena, 3) thin and stable tracks, 4) high energy which leads to distortions and 5) too thick track due to keyhole melting mode. Kempen et al [15] defined a process window for AlSi10Mg based on four requirements for optimal SST: 1) the track must be continuous to avoid porosity in the part, 2) the track must slightly penetrates the previous layer to ensure good cohesion between layers, 3) the track must have a sufficient height to build

up the part and 4) the connection angle of the track should be about 90° to ensure a good dimensional accuracy. They showed that there is not one set of optimal L-PBF parameters but an area of optimal ones. This area lies between two linear boundaries in a graph P-v: P = v*E'$_{min}$ and P = v*E'$_{max}$ where E'$_{min}$ and E'$_{max}$ are the slope of these boundaries. The advantage of analyzing SST instead of cubes is that it is clearly less time and material consuming.

To manufacture parts based on the SST optimized parameters, the adequate hatching space (HS) needs to be determined. Indeed, if HS is too low, there is more thermal accumulation in the melt pool and the temperature increases. It causes an extra overlapping between adjacent tracks which can lead to melt flow instabilities, evaporation and an increased tendency for gas entrapment and porosities [16,17]. On the other hand, if HS is too large, there is less energy penetration per volume and the melt pool temperature decreases. It causes an insufficient overlapping between adjacent tracks which can lead to lack of fusion and increased porosity. It means that an adequate HS has to be found in between these upper and lower bounds.

The current literature does not clearly link these SST, the porosity and the static mechanical properties. Indeed, the influence of the porosity on the mechanical properties depends not only on its global volume fraction in the part but also on its size and its distribution. Moreover, Dai et al. [18] showed that the geometry of the melt pool boundary has a significant influence on the mechanical properties. The cracks initiate in the boundary between two adjacent tracks and then propagate along the boundary between two successive layers. Santos Macías et al. [19] also showed the influence of the melt pool boundary on the crack propagation and evidenced that the porosity, under an acceptable level, does not influence the static mechanical properties. However, porosity has a major influence on the fatigue behaviour [19], which is not the focus of the present study. Thijs et al. [20] showed that the fast and directional cooling rate creates a unique and fine microstructure. The solidification and the fineness of this microstructure depend strongly on the thermal gradient and the growth rate which are dictated by the L-PBF parameters [20]. This means that L-PBF parameters have a strong influence on microstructure, and so on mechanical properties of the parts.

Aluminum alloys are materials of choice for the aeronautics and automotive industries thanks to its excellent strength to weight ratio [21]. L-PBF studies have focused on Al-Si alloys because of its excellent castability and low thermal expansion coefficient. The high cooling rate of L-PBF induces a very fine microstructure which leads to excellent mechanical properties. The microstructure of the Al-Si alloys is composed of α-Al phase cells surrounded by Si-rich interconnected network. This Si-rich network is the source of damage nucleation and controls the static mechanical properties [19].

The objective of this study is to develop a methodology for the efficient optimization of the L-PBF parameters in order to build dense parts with excellent mechanical properties. This methodology is here validated on the AlSi12 alloy.

Nomenclature and units

d	Depth of a single scan track [μm]
E_L	Linear energy density [J/mm]
h	Height of a single scan track [μm]
HS	Hatching space [μm]
L	Half width of a single scan track [μm]
P	Laser power [W]
t	Layer thickness [μm]
v	Scanning speed [mm/s]
W	Width of a single scan track [μm]
x	Minimal overlapping distance between two adjacent single scan tracks [μm]
ε_f	Fracture strain []
θ	Contact angle of a single scan track [°]

ρ   Density [g/cm^3]
σ$_Y$ Yield strength [MPa]
σ$_{UTS}$ Ultimate tensile strength [MPa]

Abbreviations

CCD   Central composite design
DOE   Design of Experiments
Factorial DOE Full factorial design
L-PBF   Laser powder bed fusion
RSM   Response surface method
SLM   Selective Laser Melting
SST   Single scan track

2. Materials and methods

2.1. Material

The material used in this study is gas atomized AlSi12 powder provided by 3D Systems. The chemical composition of the powder is provided in Table 1. The particle size, measured by laser diffraction granulometry in a wet dispersion (machine Coulter LS100Q), is between 6.7 μm (D10) and 35.2 μm (D90) with an average size of 22 μm.

2.2. Methodology

The four steps of the methodology which will be validated in this study are schematized in Fig. 1: (1) Design of experiments (DOE), (2) Samples manufacturing, (3) Characterization and (4) Statistical analysis and parameters selection. Each of these steps will be further detailed in the following sections.

2.3. Design of experiments (DOE)

During this first step, a DOE is performed in order to select the L-PBF parameters of the SST of Batch 1. In this study, two different kind of DOE are compared: a Central Composite Design (CCD) (see Fig. 2) and a Full Factorial Design (Factorial DOE) [22]. The goal is to validate the use of a CCD in the methodology. Indeed, in this way, it will be possible to conclude if the limited number of experiments of the CCD leads to a similar parameter selection as when running all the experiments like in the Factorial DOE. This would clearly decrease the experimental cost. The software JMP Pro version 14.3.0 is used to perform the DOE.

There are two relevant factors for the SST analysis, which are P and v. Buchbinder et al. [23] stated that due to the high reflectivity and thermal conductivity of Aluminum, the minimal laser power required to manufacture dense parts is 150 W. Hence, in this study, the laser power is varied over a wide range from: 164 W to 273 W (the upper limit of the available L-PBF machine). The scanning speed is also varied over a wide range: from 500 to 2500 mm/s. Therefore, E$_L$ ranges from 65.6 to 546 J/m (using Eq. 1).

The responses of interest are the geometric features of the SST (see Fig. 3). From the top view, the continuity of the track is analyzed as a categorical response which takes the value "yes" if the track is continuous and "no" if it is not. From the cross section analysis, the contact angle θ is an important response to ensure a good accuracy and high density [15]. According to Ansari et al., its value should be in the range from 50 to 80° [24]. The last response of interest is the ratio 100*d/(h+d) which represents the percentage of depth over the total height of the track. This parameter will ensure that the melting occurs in conduction mode and not in keyhole mode, that there is enough penetration of the previous layer to ensure a good cohesion between layers and that there is a sufficient height of the track to efficiently build the part.

The Factorial DOE consists of analyzing all the combinations of levels of P and v. There are five levels of P: 164, 191, 218, 246 and 273 W and 21 levels of scanning speed: from 500 to 2500 mm/s by steps of 100 mm/s, which means that the Factorial DOE analyzes 105 combinations altogether.

Finally, the CCD which is the most popular design of response surface methodology (RSM), consists in a mathematical and statistical technique which produces a model between the responses and the factors of a problem. Its goal is to optimize the response of interest [5]. It is composed of four axial points (in grey), four factorial points (in black) and one center point (in white) used to estimate the error, see Fig. 2. The two factors P and v are both divided in five levels: (−α, −1, 0, 1, α). In the present study, α is equal to two in order to vary each factor over five levels: for P: 164, 191, 219, 246 and 273 W and for v: 500, 1000, 1500, 2000 and 2500 mm/s. This DOE results in nine combinations altogether which are detailed in Table 2.

2.4. Samples manufacturing

The second step of the procedure consists in manufacturing the samples. The L-PBF equipment used in this work is the ProX200 L-PBF machine from 3D Systems. It uses a laser with a wavelength of 1070 nm and a power up to 273 W. All samples were built under argon atmosphere with a maximum oxygen content of 500 ppm. The building plate was not heated. This second step is divided into three sub-steps: manufacturing of Batch 1) SST, Batch 2) cubes and Batch 3) tensile samples.

SST were built on an AlSi12 substrate built with the parameters advised by the machine manufacturer: $P = 205$ W, $v = 1200$ mm/s, HS = 100 μm and $t = 30$ μm. The L-PBF parameters used for the SST are determined by the DOE. The layer thickness was kept constant at 30 μm. When the layer is thick, large powder particles are in the powder bed and can entrap porosity around them. In thin layers, these large particles are removed out of the powder bed by the recoater roller which leads to higher powder bed density [25]. Therefore, a compromise in layer thickness should be made to ensure compact powder bed while not wasting too much powder. Based on the granulometry results, 30 μm were chosen for the layer thickness and will not be varied in the present work.

Cubes of 10 mm size were built with the L-PBF parameters of interest selected based on the SST. Tensile samples of 100x12x1.5 mm^3 were manufactured horizontally (tensile direction perpendicular to the building direction) by L-PBF. Then, they were machined by electrical discharge machining (EDM) according to ASTM-E8M i.e. thickness, reduced section length and width are 1.5 mm, 26 mm and 6 mm respectively (see all dimensions in Supplementary materials).

2.5. Characterization

The third step of the procedure consists of the experiments and the characterization of the manufactured samples of the different batches.

First, the top views of the SST of Batch 1 were analyzed by scanning electron microscopy (SEM ZEISS FEGSEM ultra 55) with a focus on their width and their continuity. However, such an analysis is also possible by classical optical microscopy. Then, the SST were cut perpendicular to the track length. Their cross sections were polished to mirror-like surface and observed by SEM. The geometrical data introduced on Fig. 3 were measured with the software ImageJ three times on two different transverse cuts for each SST and were averaged.

Following SST analysis, the density of the cubes was measured by Archimedes method according to the ASTM-B311. This is a non-destructive technique which allows the determination of the density

Table 1
Chemical composition of the AlSi12 powder measured by inductively coupled plasma.

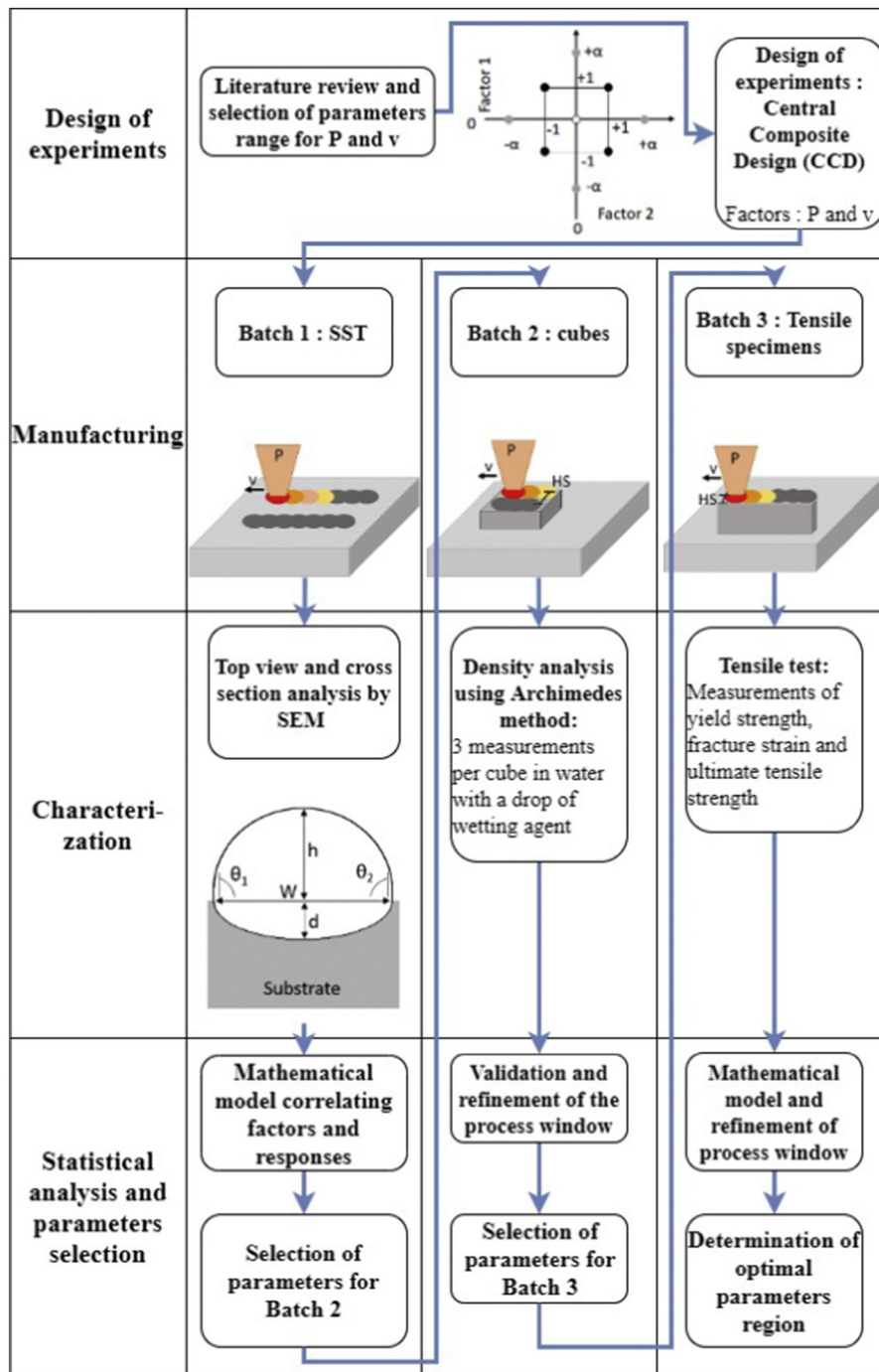| Al	Mg	Si	Ca	Fe	K	Na
88.97	<0.01	10.7	0.05	0.17	0.03	0.07

Fig. 1. Methodology to optimize the L-PBF parameters of a new powder and/or in a new L-PBF machine in order to manufacture dense parts with optimized mechanical properties.

based on the fact that the volume of the displaced fluid is equal to the immersed volume of the body [26]. Additional details about the method are provided in the Supplementary materials. A Mettler Toledo AE200 weighing system was used.

Three different liquids were employed in order to study the influence of the liquid on the accuracy of the measurement and validate the choice of water with wetting agent in the methodology: ultrapure water, ultra-pure water with a drop of wetting agent (water with 10–20% of sodium laureth sulfate and 1–5% of lauramine oxide) and ethanol. Fig. 4 shows the box plots of the standard deviation of density measurements (using Archimedes method) in function of the used

liquid. It is a graphical tool, which shows the distribution of data. The box contains the interquartile range (middle 50% of the data) and the horizontal line inside the box is the median [5]. The whiskers show the minimal and maximal values and the individual points are outliers. It can be seen that the densities measured in water have the highest standard deviation with a median of 0.0019 g/cm³, then ethanol with 0.0012 g/cm³ and finally, water with a drop of wetting agent with 0.0004 g/cm³. It means that water gives the less reproducible measurements but adding a drop of wetting agent makes it the most reproducible liquid for this measurement. Indeed, water has a high surface tension which promotes the adherence of bubbles on the sample
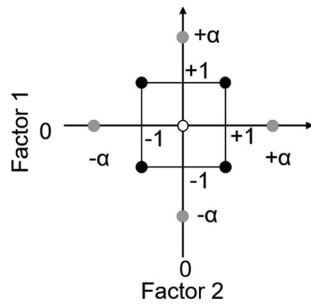
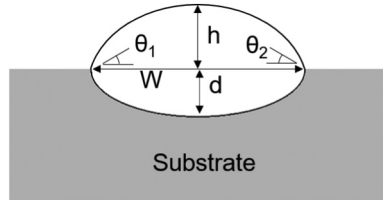**Fig. 2.** Schematic representation of a central composite design to study two factors of five levels.

Fig. 3. Schematic representation of the cross section of a single scan track reporting measured geometrical features.

Table 2
Experimental design matrix obtained by CCD.

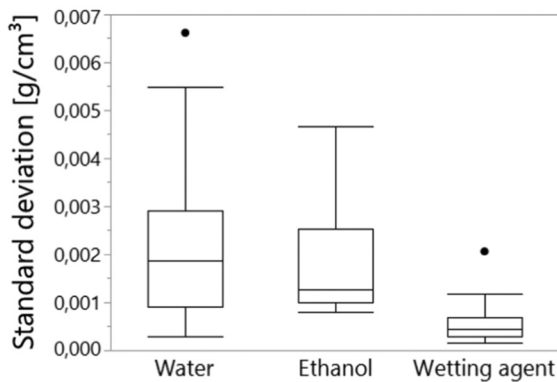| Run	P [W]	v [mm/s]
1	164	1500
2	191	1000
3	191	2000
4	218	500
5	218	1500
6	218	2500
7	246	1000
8	246	2000
9	273	1500

Fig. 4. Box plots of the standard deviations of the Archimedes density results for ultra-pure water, ethanol and ultra-pure water with a drop of wetting agent. The samples studied here are the cubes of Batch 2.

surface. However, the buoyancy of a bubble of 1 mm of diameter is about 0.5 mg while a bubble of 2 mm would have a buoyancy of 4 mg [27]. These bubbles have a non-negligible influence on the results, this is why decreasing the surface tension of the water by the addition of a drop of wetting agent significantly improves the reproducibility of the results. Thus, the reader that applies the proposed methodology

described in Fig. 1 is also advised to use water with a drop of wetting agent for Archimedes density measurements. The results of Fig. 4 confirm indeed the reliability and reproducibility of this measurement. In this study, all the density results were measured in water with a drop of wetting agent.

Uniaxial tensile tests were performed according to ASTM-E8M – 15a standard using a Zwick/Roell 50 kN tensile machine. Three samples were tested for each set of L-PBF parameters and their results were averaged.

2.6. Statistical analysis and parameters selection

The last step of the methodology consists in a statistical analysis of the characterization results and the selection of the L-PBF parameters for the following batch or the optimal parameters.

Logistic regressions and ANOVA analysis are used to identify the significant L-PBF parameters and their significant interactions. It allows to evaluate the correlation between the categorical or continuous factors and the responses denoted Y and generally expressed by Eq. 2 [22].

$$Y = \beta_0 + \beta_1 X_1 + \beta_2 X_2 + \beta_{12} X_1 X_2 + \beta_{11} X_1^2 + \beta_{22} X_2^2 \tag{2}$$

where β_0, β_1, β_2, β_{11}, β_{12}, β_{22} are the model coefficients and X_1 and X_2 the two factors of interest. Then, a desirability criterion is identified and the factors are optimized.

For the selection of the parameters for Batch 2, the CCD parameters of Table 2 are always part of the selection. Moreover, three other combinations of P-v are chosen: one optimized combination per middle level of P, which are the levels: −1, 0 and 1.

After the selection of the P-v combinations, the HS and so the overlap between adjacent tracks needs to be determined. In order to avoid the formation of lack of fusion defects between tracks, the minimal overlap is a remelting of the previous track over the whole layer thickness. Therefore, if the melt pool is assumed to have an elliptical shape for the optimized SST, the length x [µm] over which the next track should overlap is given by Eq. 3 where L is half of the width of the melt pool [µm], d the depth of the melt pool [µm] and t the layer thickness [µm].

$$x = L - \sqrt{L^2 - d2} - \frac{-d\sqrt{L^2 - d^2} + L\sqrt{d^2 - t^2}}{d} \tag{3}$$

The demonstration of this equation can be found in the Supplementary materials. Therefore, the minimal overlap percentage is given by Eq. 4 and the maximal HS by Eq. 5.

$$Overlap_{min} = x/L \tag{4}$$

$$HS_{max} = (1 - Overlap_{min}) * 2L \tag{5}$$

Note that for the nine CCD combinations, the shape of the melt pool of the SST might be far from perfect ellipses. Indeed, if balling (see Introduction) is occurring the penetration can be really low while if it is a keyhole track (see Introduction), the melt pool is deep and V-shaped. Eqs. 3, 4 and 5 are no more valid for these "non-elliptical" geometries, therefore to ensure enough overlapping, a HS of 2/3 of the melt pool width is selected for the nine CCD combinations [28]. The three other P-v combinations are selected in the process window and should therefore give elliptical melt pools. Their HS has to be varied over three levels in order to draw conclusions on the influence of HS on the responses of interest and the highest level is HS_{max} determined by Eq. 5. It means that 18 combinations of P-v-HS will be used to manufacture cubes. It will allow analyzing the influence of HS on the porosity.

Finally, for Batch 3, the conclusions drawn by the density analysis allow to refine the process window. Indeed, as highly porous samples would expectedly have a low ductility, the number of samples manufactured at this step can be reduced. Only the 12 best P-v-HS combinations, including the CCD parameters, are selected to manufacture

the plates (see Table 2). This selection ensures an accurate prediction of the mechanical properties in the whole range of the tested L-PBF parameters with an increased accuracy in the process window, which is the area of interest.

3. Results and discussion

3.1. SST analysis

The top view and cross section of the SST were analyzed and the results for the CCD parameters are provided in Table 3. For low values of E_L, the SST are not continuous because too low energy penetrates the substrate to fully melt the powder and because the balling phenomenon is observed (see Fig. 5d) [29]. This non-continuity induces higher values of standard deviations for θ and 100*d/(d+h) (see Table 3). For large values of E_L (see Fig. 5a), an increase of the ratio 100*d/(d+h) and a decrease of θ are observed.

Four types of SST were identified and can be observed on Fig. 5. The L-PBF parameters of these SST images belong to the Factorial DOE and not the CCD as they are the most representative of each type of SST. For high E_L, large, deep V-shaped and porous tracks are observed. This is characteristic of a transition from conduction to keyhole mode. The convection flow reverses inside the melt leading to the collapse of the melt pool sidewalls [30]. More gas bubbles are trapped in the melt pool and large pores are formed at the bottom of the melt pool. This keyhole track (see Fig. 5a) is not desirable in our methodology due to its increased porosity level.

When E_L is decreased, the melting mode becomes a conduction mode but the track is irregular (see Fig. 5b). At high P and low v, the temperature inside the melt pool is increased leading to a less viscous liquid, remaining liquid for a longer time [14]. This excessive liquid formation enhanced by the Marangoni effect leads to the formation of small balls [31]. It is called self-balling. It can cause an increased surface roughness, porosity formation and delamination due to poor inter-layer cohesion [32]. Moreover, this excessive liquid formation leads to a track of insufficient height (lower than the layer thickness). If the tracks are not high enough, the part will not be built accurately [15]. This type of track is therefore not desired to build dense parts.

When the energy is further decreased, the SST becomes stable and continuous (see Fig. 5c). The height is sufficient to build the part and the depth allows a good cohesion with the previous layer. It is this type of track which is desired to manufacture dense parts with sound mechanical properties and which will be the focus of the proposed methodology.

Finally, when E_L is too low, the SST becomes a discontinuous series of drops due to poor wetting of the melt [32] (see Fig. 5d). The depth of this type of track is too low to induce a good cohesion with the previous layer: this corresponds to a balling phenomenon [29]. In conclusion, the parameters leading to a stable track (see Fig. 5c) needs to be investigated in order to manufacture dense parts with sound mechanical properties. The desirability criteria corresponding to this stable case can be described as a continuous track with a contact angle as close as possible to 90° and 100*d/(d+h) between 20 and 60%.

3.2. SST based process window

A mathematical model to correlate P and v to the responses (continuity, θ and 100*d/(d+h)) is developed for the CCD and for the Factorial DOE. First, a logistic regression is performed for the correlation of the categorical response "continuity" with P, v and their interaction P*v. For both DOE, the p-values of the individual factors P and v are smaller than 0.05 but the one of the interaction P*v is 0.99. The null hypothesis states that the factors do not have a significant influence on the response. This p-value represents the probability that the observed value is obtained if this null hypothesis is true [5]. As a significance level of 0.05 is commonly chosen, it means that factors such as P and v, which have a p-value smaller than 0.05, have a significant effect on the continuity but nothing can be said for the interaction P*v. The p-value of the model obtained for the Factorial DOE and the CCD are smaller than 0.0001 and 0.0085 respectively. This means that both models are significant to predict the responses in function of P and v and the probability to obtain a continuous SST is defined in Eqs. 6 and 7 for the Factorial DOE and CCD respectively. These equations will be used later to plot Fig. 6.

An analysis of variance (ANOVA) is used to correlate the two factors and their interactions to the numerical continuous responses θ and 100*d/(d+h). The results are provided in Table 5 for both designs. It can be observed that P, v and P^2 have a significant influence on the responses (p-value < 0.05). No lack of fit can be emphasized (p-value > 0.05). The R^2 values (measure of the quality of the fit of the model) indicate that the models reasonably fit the relationship between the factors and the responses. The equations to model θ and 100*d/(d+h) are provided in Table 4 (Eqs. 8–11).

Fig. 6 shows the process window obtained using the Factorial DOE and CCD. The red, dotted and blue areas correspond to the L-PBF parameters which lead to non continuous track, inadequate contact angle (< 50° or > 100°) and inadequate 100*d/(d+h) (< 20% or > 60%) respectively. The red area of Fig. 6 corresponds thus to balling tracks (see Fig. 5d). The lower blue and dotted area correspond thus to irregular and keyhole tracks (see Fig. 5c). It means that the white area contains the L-PBF parameters which lead to satisfying stable SST and is therefore called the process window. It is worth noting that 85% of the process window defined by the Factorial DOE is also considered as process window in the CCD. The upper (red) boundary of the process window is only shifted by 140 mm/s between Fig. 6a and Fig. 6b. The process window allows thus higher scanning speed with the CCD methodology. Notice that the models are generally expected to be less accurate on their boundaries [5]. Since the Factorial DOE is using more data than the CCD, it is clear that the CCD based predictions (see Fig. 6b) are less accurate especially on the domain boundaries. Indeed, the process window is incorrectly wider for the lowest and highest laser powers. Therefore, the reader is advised not to select process parameters for batch 2 and 3 on the domain boundaries.

Fig. 7 shows the continuity, θ and 100*d/(d+h) in function of P and v for both DOE based on the equations in Table 4. The predicted responses are very similar for both models. The continuity and the ratio 100*d/(d+h) of the SST increase when P increases and v decreases. Indeed, when E_L increases, more powder is melted which leads to more continuous and deep tracks. θ shows the opposite trend which is in good agreement with the observations of Fig. 5. For low v and high P, θ is really low (close to 30°) and 100*d/(d+h) is high. This corresponds to keyhole tracks (see Fig. 5a). When the SST are not continuous (in blue on Fig. 7(a, b)), it corresponds to balling tracks (see Fig. 5d).

As the CCD reasonably fits (85%) the Factorial DOE (see Fig. 6 and Fig. 7), only the CCD will be considered for the rest of this study. The CDD, based on only nine SST, already gives a really good approximation of the process window.

Table 3
Measurements of continuity, θ and 100*d/(d+h) for the nine parameter combinations of the CCD based on the top view and cross section analysis observed by SEM.

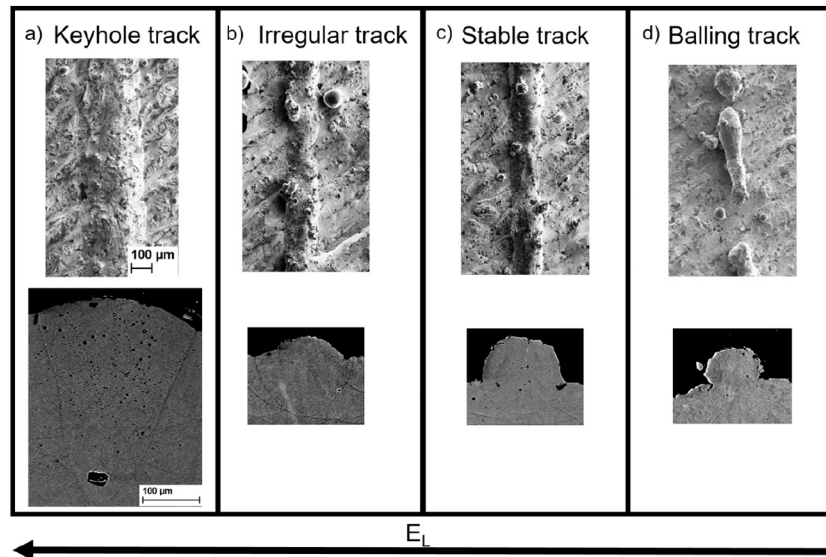| P [W]	v [mm/s]	E_L [J/mm]	Continuity	θ [°]	$\frac{d}{d+h}$*100 [%]
164	1500	109	Yes	80 ± 5	38 ± 3
191	1000	191	Yes	61 ± 19	60 ± 3
191	2000	95.5	No	65 ± 15	50 ± 13
218	500	438	Yes	30 ± 6	88 ± 2
218	1500	146	Yes	37 ± 14	66 ± 4
218	2500	87.6	No	86 ± 19	46 ± 9
246	1000	246	Yes	45 ± 19	73 ± 9
246	2000	123	Yes	47 ± 14	52 ± 1
273	1500	182	Yes	55 ± 11	57 ± 2

Fig. 5. SEM images of the top views and cross sections of the four types of SST in function of E_L. The L-PBF parameters are a) P= 273 W and v= 600 mm/s, b) P= 218 W and v= 1300 mm/s, c) P=218 W and v=1600 mm/s and d) P= 164 W and v=2400 mm/s.

For Batch 2, the nine CDD parameters of Table 2 are chosen with HS=2/3 * W as stated by the proposed methodology (see Fig. 1) [28]. Moreover, one combination of parameters is chosen in the process window (white area on Fig. 6b) for P=191, 218 and 246 W (not at the domain boundaries of the model) based on the desirability criteria i.e. the track needs to be continuous, θ has to tend to 90° and 100*d/(d+h) needs to tend to 45% in the rang 30 to 60%. The L-PBF combinations are provided in Table 6.

3.3. Cubes characterization

Density measurements are provided in Table 6 and Fig. 8. The process window obtained based on the CCD and SST analysis (white area on Fig. 8) includes the highest measured densities and mainly close to the upper boundary of the process window (near the red zone corresponding to the boundary between continuous and non continuous tracks) which validates the use of SST to have a first insight of the L-PBF parameters of interest. The lowest density (in red in Table 6) is obtained for the parameters P = 218 W, v = 500 mm/s and HS = 180 μm which corresponds to very high E_L of 436 J/mm. As the depth-

Table 4
Prediction equations of continuity, 100* d/(d+h) and θ for the Factorial DOE and the CCD.

Factorial DOE	CCD
$P(yes) = \dfrac{e^{-545.14+4.44*P-0.81*v}}{1 + e^{-545.14+4.44*P-0.81*v}}\#(6)$	$P(yes) = \dfrac{e^{-82.7+0,8*P-0,1*v}}{1 + ae^{-82.7+0,8*P-0,1*v}}\#(7)$
$\dfrac{100\,d}{d+h} = 42.7 + 0.2*P$	$\dfrac{100\,d}{d+h} = 58.4 + 0.2*P-0.02*v$
$-0.02*v-0.003*(P-217.5)^2\#(8)$	$-0.006*(P-218.5)^2\#(9)$
$\theta = 61.8-0.2*P+0.02*v$	$\theta = 77.2-0.3*P+0.02*v$
$-0.003*(P-217.5)^2\#(10)$	$+0.006*(P-218.5)^2\#(11)$

to-width ratio of the SST i.e. 249/260 = 0.95 is higher than 0.5, it means that the melting mode is a keyhole mode [33]. This explains the higher porosity compared to the other parameters. Indeed, the high energy density induces an increase of the temperature of the melt pool, leading to increased recoil pressure, vaporization of material and increased gas bubbles entrapped in the melt pool leading to porosity [34]. It can also be observed that combinations of parameters with
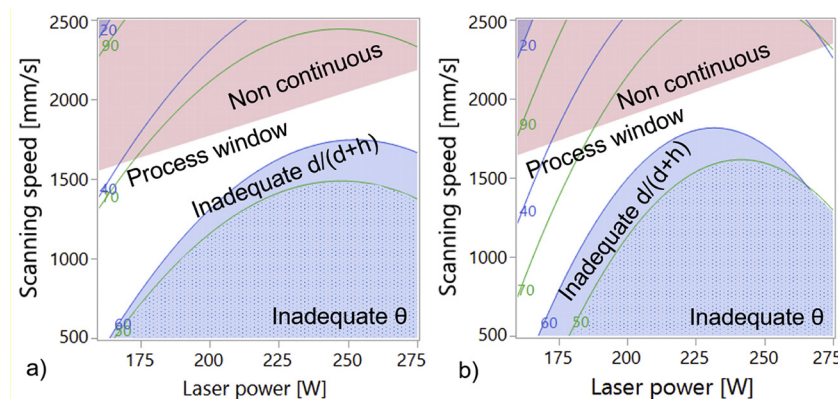
Fig. 6. Process window in function of P and v obtained based on the a) Factorial DOE and b) CCD. The white region corresponds to the parameters leading to adequate responses (continuous, contact angle between 50 and 100° and 100*d/(d+h) between 20 and 60%). The red, blue and dotted regions represent the non continuous, inadequate d/(d+h) and inadequate contact angle respectively. The blue and green lines represent the isoresponses for d/(d+h) and the contact angle respectively. (For interpretation of the references to color in this figure legend, the reader is referred to the web version of this article.)

Table 5

ANOVA results for 100*d/(d+h) and θ for both DOE including the p-values of the factors and their interactions, the lack of fit and the fit parameters: mean, R^2, adjusted R^2 and root mean square error.

p-value	Factorial DOE		CCD	
	100*d/(d+h)	θ	100*d/(d+h)	θ
Model	$<1*10^{-4}$	$<1*10^{-4}$	$7*10^{-4}$	$5*10^{-2}$
P	$<1*10^{-4}$	$<1*10^{-4}$	$1*10^{-2}$	$4*10^{-2}$
v	$<1*10^{-4}$	$<1*10^{-4}$	$3*10^{-3}$	0.1
P^2	$<1*10^{-4}$	$4.4*10^{-3}$	$3*10^{-3}$	/
v^2	0.50	0.32	0.51	0.21
P * v	0.37	0.07	0.22	0.94
Lack of fit	0.22	0.56	/	/
Mean	56.4%	58.3 °	58.9%	56.2 °
R^2	0.8	0.51	0.96	0.61
Adjusted R^2	0.8	0.50	0.93	0.49
Root mean square error	7.9%	13.8 °	3.9%	13.3 °

Table 7

ANOVA parameters i.e. p-value of the factors and their interactions and model R^2 based on the yield strength, fracture strain and ultimate tensile strength.

Based on	σ_y	ε_{UTS}	σ_{UTS}
P	$<1*10^{-4}$	$1.0 * 10^{-1}$	0.0
v	$<1*10^{-4}$	$1.6 * 10^{-4}$	$5.0 * 10^{-5}$
P^2	$2.2 * 10^{-4}$	$1.5 * 10^{-3}$	$3.0 * 10^{-5}$
P HS	$3.5 * 10^{-3}$	$1.0 * 10^{-5}$	$1.0 * 10^{-5}$
v HS	$1.0 * 10^{-2}$	/	/
HS	$5.3 * 10^{-2}$	0.0	$4.4 * 10^{-1}$
P v	/	$1.1 * 10^{-3}$	/
v^2	/	$1.6 * 10^{-2}$	/
Model R^2	0.93	0.89	0.88

$$\rho = 100.2 - 0004 \cdot P + 0.0005 \cdot v - 0.01 \cdot HS - 0.0001 \cdot (P - 225.6) \cdot (HS - 92.2)$$
$$+ 0.00002 \cdot (v - 1591) \cdot (HS - 92.2)$$

(12)

high HS (see Table 6), show a higher porosity level in the cubes compared to lower HS cases. It can be due to an insufficient overlap between adjacent tracks leading to lack of fusion defects between them.

Indeed, Eq. 5 assumed that the geometry of the SST is perfectly elliptical which is not what is actually observed even for stable tracks (see Fig. 5c). The difference is even more evident for the geometry of balling, irregular and keyhole tracks (see Fig. 5d, Fig. 5b and Fig. 5a respectively). It is therefore advised to the reader who wants to use the methodology to prefer low HS values, at least lower than HS_{max} (see Eq. 5) in order to improve the density of the cubes and to limit the use of Eq. 5 for stable tracks.

An ANOVA analysis is performed in order to correlate the factors P, v, HS and their interactions with the densities of the cubes. It is evidenced that v*HS, HS, v, P and P*HS have a significant influence on the porosity (p-value < 0.05). R^2 is 0.98 which translates an excellent quality of the fit. Eq. 12 is the prediction expression of the density where ρ is the density [g/cm³], P the laser power [W], v the scanning speed [mm/s] and HS the hatching space [μm].

Fig. 9 shows the parts density in function of P and v for four values of HS according to Eq. 12. It can be observed that the density increases when P decreases and v increases, i.e. E_L increases. Moreover, the density increases when HS decreases. Indeed, when HS decreases the overlap between SST increases and there is no more lack of fusion defects between SST. Moreover, the higher thermal energy accumulation induces an increase of the temperature inside the melt pool which improves the liquid spreading and so the wetting of the surrounding powder particles [17]. When HS decreases, the process window leading to the same density is wider. Indeed, the white region corresponds to densities higher than 99.2%. It can be noticed that this model does not consider the balling phenomenon. Indeed, Fig. 9a suggests that a combination of parameters P=164 W, v=2400 mm/s and HS=75 μm would lead to a part density higher than 99.4%. However, Fig. 5 shows that the same combination of parameters P=164 W and v =2400 mm/s leads to a balling track (Fig. 5d) which is clearly not continuous. Li et al. showed that the HS has no influence on the balling phenomenon [32], which means that balling phenomenon would occur for any

Table 6

Results of cubes density obtained by Archimedes density method. The dark green contains the values higher than 99.3%, light green between 99% and 99.3%, the orange between 98% and 99% and the red lower than 98%. The results of the tensile tests of Batch 3 are in the three last columns. For the yield strength, the dark green color contains the values higher than 300 MPa, light green between 280 and 300 MPa, the orange between 250 and 280 MPa and the red lower than 250 MPa. For the fracture strain, the dark green color contains the values higher than 9%, light green between 8 and 9%, orange between 7 and 8% and red lower than 7%. For the σ_{UTS} [MPa], the dark green contains the values higher than 500 MPa, light green between 480 and 500 MPa, the orange between 450 and 480 MPa and red lower than 450 MPa.

P [W]	v [mm/s]	HS [μm]	ρ [%]	σ_Y [MPa]	ε_f [%]	σ_{max} [MPa]
164	1500	70	99.42 ± 0.01	316.8±0.4	9.3±0.3	520.9±1.5
191	1000	115	99.00 ± 0.02	270.8±2.4	8.9±2.0	477.0±3.4
191	1400	75	99.23 ± 0.02	/	/	/
191	1400	85	99.21 ± 0.01	298.9±2.3	9.3±0.4	503.8±8.3
191	1400	100	98.9 ± 0.01	/	/	/
191	2000	60	98.94 ± 0.02	314.6±0.8	9.4±0.3	519.1±3.7
218	500	180	95.8 ± 0.03	/	/	/
218	1500	100	99.02 ± 0.02	276.33±8.6	8.9±0.4	471.9±17.3
218	1600	75	99.42 ± 0.03	/	/	/
218	1600	100	99.07 ± 0.01	288.0±2.4	8.4±0.4	484.7±7.9
218	1600	125	98.94 ± 0.01	299.0±1.9	6.8±0.3	479.8±3.5
218	2500	60	99.51 ± 0.01	306.5±6.5	8.95±0.3	509.0±5.1
246	1000	135	97.84 ± 0.04	222.7±11.6	5.8±1.3	393.7±31.6
246	1800	60	99.45 ± 0.02	/	/	/
246	1800	85	99.27 ± 0.02	287.9±1.4	9.0±0.5	493.4±1.8
246	1800	125	98.85 ± 0.01	/	/	/
246	2000	75	99.32 ± 0.02	299.9±1.7	9.3±0.2	506.2±6.1
273	1500	75	99.26 ± 0.08	272.2±15.3	9.4±0.3	477.8±16.2

Table 8

Comparison of the experimental and the CCD predicted properties for the L-PBF parameters P=164 W, v=1000 mm/s and HS=90 μm.

	Continuity	θ[°]	100d/(d+h)[%]	ρ[%]	σ_y [MPa]	σ_{UTS} [MPa]	ε_f [%]
Predicted	Yes	71	47	99.15±0.1	306.9±14.7	522.2±25.4	9.5±0.8
Exp	Yes	69±10	52±2	99.2±0.0	300.6±2.7	504.3±2.0	9.2±0.3

Table 9

Comparison of the tensile properties of L-PBF AlSi12 obtained in this study with the ones reported in the literature.

P [W]	v [mm/s]	t [μm]	HS[μm]	σ_Y [MPa]	σ_{UTS} [MPa]	ε_f [%]	Build direction	Source
/	/	/	/	220.5±9.4	418.9±9.6	3.91±0.27	/	[42]
400	1000	30	60	315.5	476.3	6.7	Horizontal	[18]
300	500	50	45	/	325	4.4	Horizontal	[43]
320	1455	50	110	200±2	410±4	6.6±0.5	/	[44]
285	1500	40	100	224.8±33.5	398.6±16.5	3.42±0.04	/	[45]
320	1455	50	110	270.1±10	325±20	4.4±0.7	/	[46]
164	1500	30	70	316±0.4	520.9±1.5	9.3±0.3	Horizontal	Present work

value of HS. Balling phenomenon is known to be a defect which increases the porosity and surface roughness [35]. Therefore, the density model should be combined with the SST models.

Now, the 12 combinations of L-PBF parameters for the tensile tests need to be selected. First, the nine combinations of parameters of the CCD (see Table 2) are chosen except the combination P = 216 W, v = 500 mm/s and HS = 180 μm due to its too low density (see Table 6) which would expectedly lead to low ductility. Four other combinations of high density parameters need to be selected among the other batch

two cubes parameters. Moreover, the parameters P = 218 W, v 1600 mm/s and HS = 125 μm are selected to analyze the influence of HS on the mechanical properties. The final selection is provided in Table 6.

3.4. Tensile tests

The tensile properties for the selected L-PBF parameters are provided in Table 6. The full tensile curves are provided in the Supplementary materials. The highest yield strength are obtained for the lowest
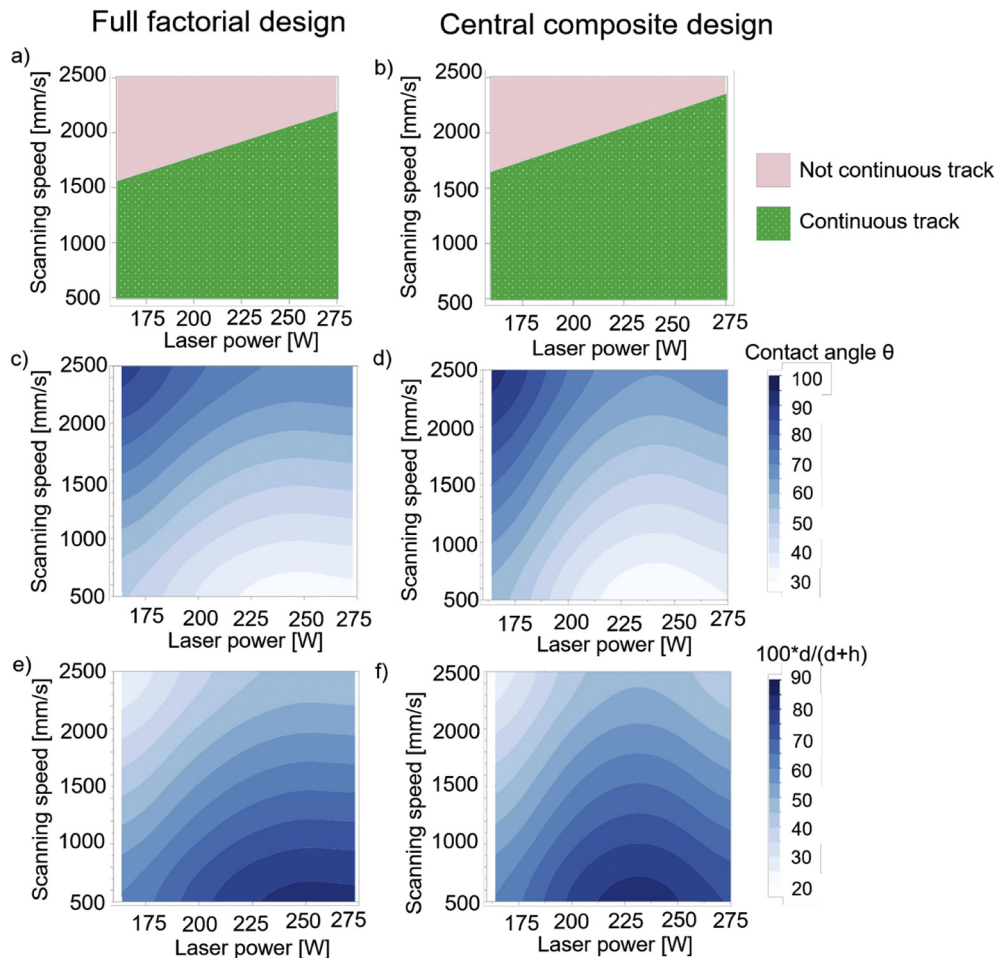

Fig. 7. (a,b) Continuity in function of P and v, (c,d) 100*d/(d+h) in function of P and v and (e,f) the contact angle in function of P and v. These are calculated for (a,c,e) the factorial DOE and (b,d,f) the CCD using parameters of Table 2.
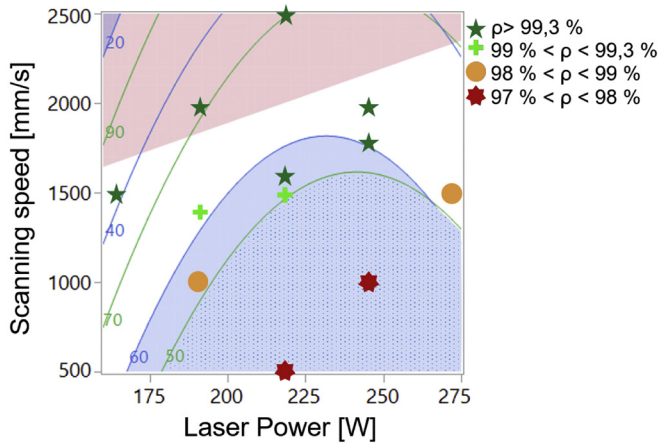
Fig. 8. Cubes density for various L-PBF parameters in the process window with HS = 2/3 W superimposed on Fig. 6b (see that figure for the color code).

laser power P. Indeed, decreasing P results in higher cooling rate and thinner microstructure [36]. The fracture strain increases when P increases and, v and HS decrease, in a similar way than the porosity (see Fig. 9). It is expectedly this higher porosity which decreases the fracture strain [37].

The lowest ductility of Batch 3 (in red and orange of Table 6) are corresponding to the combinations P=246 W-v=1000 mm/s-HS=135 μm and P=218 W-v=1600 mm/s-HS=125 μm. This is due to their higher porosity level compared to the other combinations (see Table 6) while the highest mechanical properties (in dark green) are obtained for the highest density parameters [38].

The results of the ANOVA analysis are provided in Table 7. It can be seen that many parameters and their interaction have a significant influence on the mechanical properties (p-values < 0.05). HS is the parameter that has the most significant influence on the fracture strain. Indeed, a large HS can lead to lack of fusion defects and thus, decrease the fracture strain. The contributions of P and v more significantly affect for the yield strength and the ultimate tensile strength. Indeed, they determine the amount of energy transmitted to the powder bed and so the microstructure thinness [36].

Fig. 10 combines all the models developed in this study for four HS values (HS=75, 85, 100 and 125 μm). The dashed green region is the optimized parameters area. The desirability criteria is the combination of a continuous track, θ higher than 50°, 100*d/(d+h) between 20 and 60%, density higher than 99%, fracture strain higher than 9%, yield strength higher than 300 MPa and ultimate tensile strength higher than 500 MPa. It is important to combine all the models and results. Indeed, if we focus on the density or tensile models, parameters leading to balling phenomena could have been selected.

In order to validate the model, a combination of L-PBF parameters which fulfils all the desirability criteria has been selected to manufacture SST, cubes and tensile samples. This combination is $P = 164$ W, $v = 1000$ mm/s and HS = 90 μm. The experimental values obtained for this parameters combination are compared to the predicted values of the model in Table 8. It shows that the track geometry, cube density and mechanical properties predicted by the model are similar to the ones obtained experimentally. Moreover, the tensile properties obtained in this study are significantly higher than the state-of-the-art ones reported in the literature provided in Table 9.

It is know that they are many other parameters which can influence the thermal history of the material during the L-PBF process. Indeed, under fixed L-PBF parameters, a change in the shape or the size of the manufactured part can affect the thermal history and so the mechanical
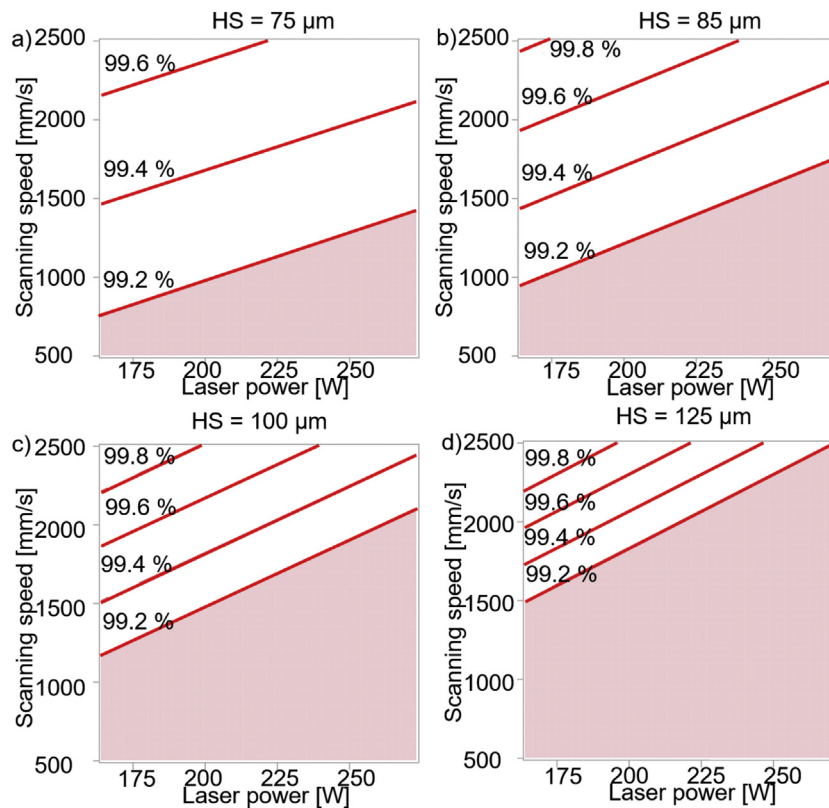

Fig. 9. Density of cubes measured by Archimedes density method for a) HS = 75 μm, b) HS = 85 μm, c) HS = 100 μm and d) HS = 125 μm. The red area contains the L-PBF parameters leading to density smaller than 99.2%. The red lines are isoresponses i.e. constant density. (For interpretation of the references to color in this figure legend, the reader is referred to the web version of this article.)
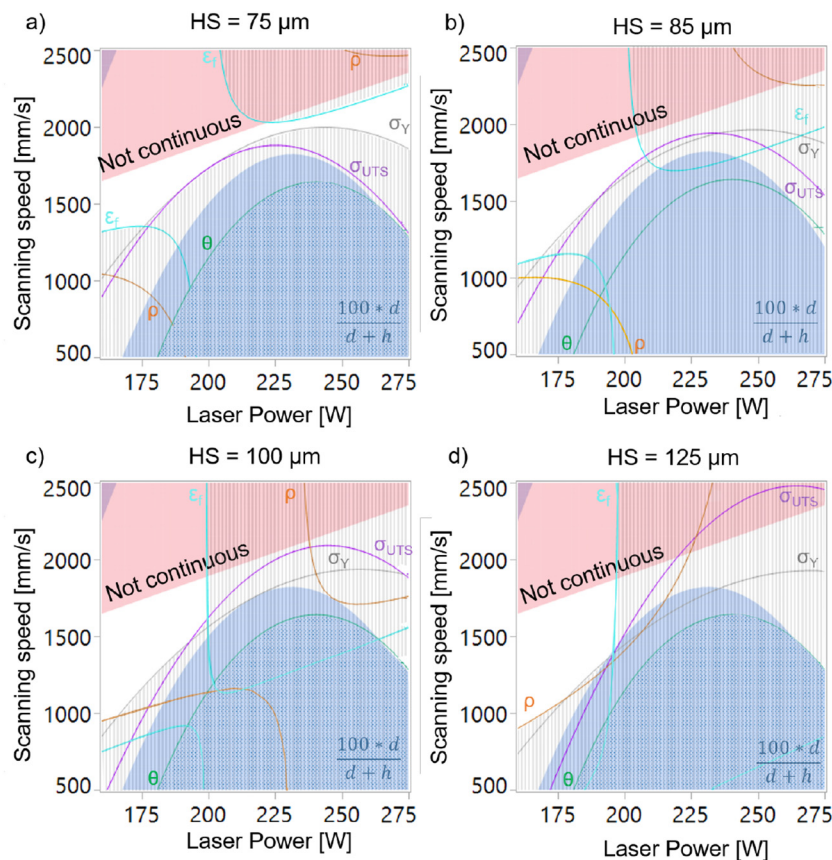
Fig. 10. Process window obtained based on all the models developed with the proposed methodology (SST, density and tensile mechanical properties) in function of P and v for a) HS = 75 µm, b) HS = 85 µm, c) HS = 100 µm and d) HS = 125 µm. The white area is the process window, while the dashed area is the zone which does not fulfill the desirability criteria for the mechanical properties and the density. The red, blue and dotted area corresponds to the parameters leading to non continuous tracks and inadequate 100*d/(d+h) and contact angle, respectively. (For interpretation of the references to color in this figure legend, the reader is referred to the web version of this article.)

properties and the density of the final part [39]. Indeed, the time interval between two successive layers deposition influences the thermal history [40]. When this interval increases, the cooling rate decreases leading to thinner microstructure, higher strength and lower fracture strain. The building orientation also affects the mechanical properties as defects are mainly present between layers. It provides an easier path for void growth when the tensile direction is perpendicular to the layer boundaries [41]. Many variations in the process can influence the thermal history and so the density and the mechanical properties. Therefore, robust L-PBF parameters need to be selected in order to minimize the effect of these variations on the quality of the part. These L-PBF parameters naturally lie in the middle of the process window. If we take the process window where HS = 100 µm, the parameters in the middle of the process window are $P = 182$ W and $v = 1550$ mm/s. For this parameter combination, a variation of 10% of P or 16% of v leads to properties which still fulfill the desirability criteria. It is therefore advised to the reader to select its L-PBF parameter in the middle of the process window which will lead to parts with reproducible quality and expectedly less dependent on the part geometry and other process variations.

4. Conclusion

An efficient methodology to identify optimized laser-powder bed fusion (L-PBF) parameters leading to dense and mechanically sound parts has been developed and validated on AlSi12. This methodology requires only three L-PBF batches. The first one with single scan tracks (SST) uses a limited amount of powder. The second and third ones, with cubes and tensile samples respectively, refine the process window. The following conclusions can be drawn:

1. The use of a design of experiments (DOE) allows to clearly decrease the manufacturing and characterization costs for such an optimization. Indeed, a central composite design (9 SST analyzed) reasonably leads to a similar P-v selection than a full factorial design (105 SST analyzed). 9 SST are sufficient to identify a process window providing 85% similarity in parameters selection than the 105 SST of the full factorial design.

2. The process window obtained based on the SST reliably leads to high cubes densities (> 99.3%). It confirms the relevance of the SST analysis as a first approach to define or refine the L-PBF process window.

3. The static mechanical properties of AlSi12 built with the optimized L-PBF parameters are better than the ones reported in the literature. Indeed, a yield strength of 316 MPa, an ultimate tensile strength of 520 MPa and a fracture strain of 9.3% were obtained in the present study.

4. The statistical model predictions for the density and the mechanical properties were validated experimentally for one new combination of optimized L-PBF parameters.

In conclusion, only 9 SST, 18 cubes and 12 tensile tests are required in the suggested methodology to optimize the L-PBF parameters and obtain dense and mechanically sound parts. This validated methodology can obviously be further applied to any existing or newly developed L-PBF materials.

Data availability

The authors confirm that their data are available.

Funding

Declaration of Competing Interest

The authors declare that they have no known competing financial interests or personal relationships that could have appeared to influence the work reported in this paper.

Acknowledgements

Appendix A. Supplementary data

Supplementary data to this article can be found online at https://doi.org/10.1016/j.matdes.2020.109433.

References

[1] C. Qiu, C. Panwisawas, M. Ward, H.C. Basoalto, J.W. Brooks, M.M. Attallah, On the role of melt flow into the surface structure and porosity development during selective laser melting, Acta Mater. 96 (2015) 72–79.

[2] S. Wen, C. Wang, Y. Zhou, L. Duan, Q. Wei, S. Yang, Y. Shi, High-density tungsten fabricated by selective laser melting: densification, microstructure, mechanical and thermal performance, Opt. Laser Technol. 116 (2019) 128–138.

[3] N. Read, W. Wang, K. Essa, M.M. Attallah, Selective laser melting of AlSi10Mg alloy: process optimisation and mechanical properties development, Mater. Des. (1980-2015) 65 (2015) 417–424.

[4] J.J.S. Dilip, G.D.J. Ram, T.L. Starr, B. Stucker, Selective laser melting of HY100 steel: process parameters, microstructure and mechanical properties, Addit. Manufact. 13 (2017) 49–60.

[5] D.C. Montgomery, Design and Analysis of Experiments, John Wiley & Sons, Inc., 2006

[6] L. Carter, K. Essa, M. Attallah, Optimisation of selective laser melting for a high temperature Ni-superalloy, Rapid Prototyp. J. 21 (2015) 423–432.

[7] M. Elsayed, M. Ghazy, Y. Youssef, K. Essa, Optimization of SLM process parameters for Ti6Al4V medical implants, Rapid Prototyp. J. 25 (3) (2019) 433–447.

[8] A. Pawlak, M. Rosienkiewicz, E. Chlebus, Design of experiments approach in AZ31 powder selective laser melting process optimization, Arch. Civil Mech. Eng. 17 (1) (2017) 9–18.

[9] A. Aversa, M. Moshiri, E. Librera, M. Hadi, G. Marchese, D. Manfredi, F. Calignano, S. Biamino, M. Lombardi, M. Pavese, Single scan track analyses on aluminium based powders, J. Mater. Process. Technol. 255 (2018) 17–25.

[10] F. Bosio, A. Aversa, M. Lorusso, S. Marola, D. Gianoglio, L. Battezzati, P. Fino, D. Manfredi, M. Lombardi, A time-saving and cost-effective method to process alloys by laser powder bed fusion, Mater. Des. 181 (2019) 107949.

[11] P. Gao, Z. Wang, X. Zeng, Effect of process parameters on morphology, sectional characteristics and crack sensitivity of Ti-40Al-9V-0.5Y alloy single tracks produced by selective laser melting, Int. J. Lightweight Mater.Manufact. 2 (4) (2019) 355–361.

[12] M. Guo, D. Gu, L. Xi, L. Du, H. Zhang, J. Zhang, Formation of scanning tracks during selective laser melting (SLM) of pure tungsten powder: morphology, geometric features and forming mechanisms, Int. J. Refract. Met. Hard Mater. 79 (2019) 37–46.

[13] X. Nie, H. Zhang, H. Zhu, Z. Hu, L. Ke, X. Zeng, Analysis of processing parameters and characteristics of selective laser melted high strength Al-Cu-Mg alloys: from single tracks to cubic samples, J. Mater. Process. Technol. 256 (2018) 69–77.

[14] I. Yadroitsev, A. Gusarov, I. Yadroitsava, I. Smurov, Single track formation in selective laser melting of metal powders, J. Mater. Process. Technol. 210 (12) (2010) 1624–1631.

[15] K. Kempen, L. Thijs, J. Van Humbeeck, J.P. Kruth, Processing AlSi10Mg by selective laser melting: parameter optimisation and material characterisation, Mater. Sci. Technol. 31 (8) (2015) 917–923.

[16] P. Wen, L. Jauer, M. Voshage, Y. Chen, R. Poprawe, J. Schleifenbaum, Densification behavior of pure Zn metal parts produced by selective laser melting for manufacturing biodegradable implants, J. Mater. Process. Technol. (2018) 258.

[17] M. Xia, D. Gu, G. Yu, D. Dai, H. Chen, Q. Shi, Influence of hatch spacing on heat and mass transfer, thermodynamics and laser processability during additive manufacturing of Inconel 718 alloy, Int. J. Mach. Tools Manuf. 109 (2016) 147–157.

[18] D. Dai, D. Gu, H. Zhang, J. Xiong, C. Ma, C. Hong, R. Poprawe, Influence of scan strategy and molten pool configuration on microstructures and tensile properties of selective laser melting additive manufactured aluminum based parts, Opt. Laser Technol. 99 (2018) 91–100.

[19] J.G. Santos Macías, C. Elangeswaran, L. Zhao, B. Van Hooreweder, J. Adrien, E. Maire, J.-Y. Buffière, W. Ludwig, P.J. Jacques, A. Simar, Ductilisation and fatigue life enhancement of selective laser melted AlSi10Mg by friction stir processing, Scr. Mater. 170 (2019) 124–128.

[20] L. Thijs, K. Kempen, J.-P. Kruth, J. Van Humbeeck, Fine-structured aluminium products with controllable texture by selective laser melting of pre-alloyed AlSi10Mg powder, Acta Mater. 61 (5) (2013) 1809–1819.

[21] N. Kang, P. Coddet, C. Chen, Y. Wang, H. Liao, C. Coddet, Microstructure and wear behavior of in-situ hypereutectic Al–high Si alloys produced by selective laser melting, Mater. Des. 99 (2016) 120–126.

[22] J. Goupy, L. Creighton, Introduction to Design of Experiments with JMP Examples, SAS Institute, 2007.

[23] D. Buchbinder, H. Schleifenbaum, S. Heidrich, W. Meiners, J. Bültmann, High power selective laser melting (HP SLM) of aluminum parts, Phys. Procedia 12 (2011) 271–278.

[24] M. Ansari, A. Mohamadizadeh, Y. Huang, V. Paserin, E. Toyserkani, Laser directed energy deposition of water-atomized iron powder: process optimization and microstructure of single-tracks, Opt. Laser Technol. 112 (2019) 485–493.

[25] K. Abd-Elghany, D.L. Bourell, Property evaluation of 304L stainless steel fabricated by selective laser melting, Rapid Prototyp. J. 18 (5) (2012) 420–428.

[26] T. de Terris, O. Andreau, P. Peyre, F. Adamski, I. Koutiri, C. Gorny, C. Dupuy, Optimization and comparison of porosity rate measurement methods of selective laser melted metallic parts, Addit. Manufact. 28 (2019) 802–813.

[27] R.A.D. Prabhakaran, D. Arun, V. Joshi, Curt A. Lavender, Procedure for Uranium-Molybdenum Density Measurements and Porosity Determination, United States, 2016.

[28] T. Polivnikova, Study and Modelling of the Melt Pool Dynamics during Selective Laser Sintering and Melting, EPFL, 2015 107.

[29] D. Gu, Y. Shen, Balling phenomena in direct laser sintering of stainless steel powder: metallurgical mechanisms and control methods, Mater. Des. 30 (2009) 2903–2910.

[30] K.V. Yang, P. Rometsch, T. Jarvis, J. Rao, S. Cao, C. Davies, X. Wu, Porosity formation mechanisms and fatigue response in Al-Si-mg alloys made by selective laser melting, Mater. Sci. Eng. A 712 (2018) 166–174.

[31] D. Gu, Y. Shen, Balling phenomena during direct laser sintering of multi-component Cu-based metal powder, J. Alloys Compd. 432 (1) (2007) 163–166.

[32] R. Li, J. Liu, Y. Shi, L. Wang, W. Jiang, Balling behavior of stainless steel and nickel powder during selective laser melting process, Int. J. Adv. Manuf. Technol. 59 (9) (2012) 1025–1035.

[33] K.Q. Le, C. Tang, C.H. Wong, On the study of keyhole-mode melting in selective laser melting process, Int. J. Therm. Sci. 145 (2019) 105992.

[34] J.L. Tan, C. Tang, C.H. Wong, A computational study on porosity evolution in parts produced by selective laser melting, Metall. Mater. Trans. A 49 (8) (2018) 3663–3673.

[35] D. Bourell, J.P. Kruth, M. Leu, G. Levy, D. Rosen, A.M. Beese, A. Clare, Materials for additive manufacturing, CIRP Ann. Manuf. Technol. 66 (2) (2017) 659–681.

[36] N. Shamsaei, A. Yadollahi, L. Bian, S.M. Thompson, An overview of direct laser deposition for additive manufacturing; Part II: Mechanical behavior, process parameter optimization and control, Addit. Manufact. 8 (2015) 12–35.

[37] A.M. Aboutaleb, M.J. Mahtabi, M.A. Tschopp, L. Bian, Multi-objective accelerated process optimization of mechanical properties in laser-based additive manufacturing: case study on selective laser melting (SLM) Ti-6Al-4V, J. Manuf. Process. 38 (2019) 432–444.

[38] I. Maskery, N.T. Aboulkhair, M.R. Corfield, C. Tuck, A.T. Clare, R.K. Leach, R.D. Wildman, I.A. Ashcroft, R.J.M. Hague, Quantification and characterisation of porosity in selectively laser melted Al–Si10–Mg using X-ray computed tomography, Mater. Charact. 111 (2016) 193–204.

[39] A. Yadollahi, N. Shamsaei, Additive manufacturing of fatigue resistant materials: challenges and opportunities, Int. J. Fatigue 98 (2017) 14–31.

[40] A. Yadollahi, N. Shamsaei, S.M. Thompson, D.W. Seely, Effects of process time interval and heat treatment on the mechanical and microstructural properties of direct laser deposited 316L stainless steel, Mater. Sci. Eng. A 644 (2015) 171–183.

[41] A. Yadollahi, N. Shamsaei, S.M. Thompson, A. Elwany, L. Bian, Effects of building orientation and heat treatment on fatigue behavior of selective laser melted 17-4 PH stainless steel, Int. J. Fatigue 94 (2017) 218–235.

[42] S. Siddique, M. Imran, E. Wycisk, C. Emmelmann, F. Walther, Influence of process-induced microstructure and imperfections on mechanical properties of AlSi12 processed by selective laser melting, J. Mater. Process. Technol. 221 (2015) 205–213.

[43] N. Kang, P. Coddet, L. Dembinski, H. Liao, C. Coddet, Microstructure and strength analysis of eutectic Al-Si alloy in-situ manufactured using selective laser melting from elemental powder mixture, J. Alloys Compd. 691 (2017) 316–322.

[44] K.G. Prashanth, S. Scudino, J. Eckert, Defining the tensile properties of Al-12Si parts produced by selective laser melting, Acta Mater. 126 (2017) 25–35.

[45] R. Rashid, S.H. Masood, D. Ruan, S. Palanisamy, R.A. Rahman Rashid, J. Elambasseril, M. Brandt, Effect of energy per layer on the anisotropy of selective laser melted AlSi12 aluminium alloy, Addit. Manufact. 22 (2018) 426–439.

[46] J. Suryawanshi, K.G. Prashanth, S. Scudino, J. Eckert, O. Prakash, U. Ramamurty, Simultaneous enhancements of strength and toughness in an Al-12Si alloy synthesized using selective laser melting, Acta Mater. 115 (2016) 285–294.